ACS MATERIALS LETTERS

www.acsmaterialsletters.org

Na-Rich Disordered Rock Salt Oxyfluoride Cathode Materials for Sodium Ion Batteries

Yasaman Shirazi Moghadam, Abdel El Kharbachi,* Yang Hu, Kai Wang, Stéphanie Belin, and Maximilian Fichtner

Cite This: *ACS Materials Lett.* 2023, 5, 125−132

Read Online

ACCESS | Metrics & More | Article Recommendations | Supporting Information

ABSTRACT: **The existing classes of Na-based cathode materials and their chemistries are still limited, mainly with respect to the increasing demand for alternative post-Li technologies. In this letter, a newly synthesized Na-rich disordered rock salt (DRS) oxyfluoride with the nominal composition Na_2MnO_2F is reported as a cathode candidate for Na-ion batteries (SIBs). Rietveld refinement analysis confirmed that the synthesized compound has a DRS structure with larger lattice compared to Li-rich homologues. During the first cycle, up to 1.7 Na^+/f.u. can be extracted at a slow rate, while a better capacity retention and cycling stability are obtained at high rate, reminiscent of electrode−electrolyte interaction. Further, X-ray absorption fine structure (*operando* and *ex situ*) confirmed the Mn oxidation state evolution upon cycling in agreement with the cyclic voltammetry redox profile, emphasizing the reversible Na^+ (de)insertion and change of the Mn local ordering. This work is an additional input to the limited series of cathode candidates for SIBs.**

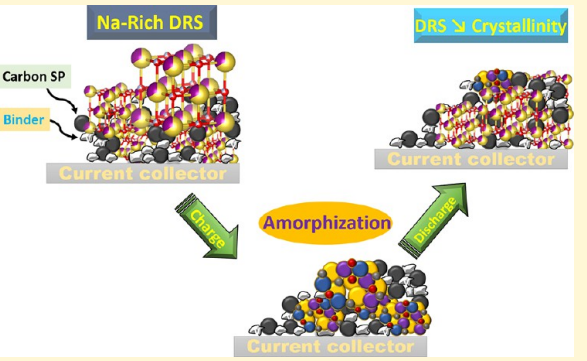

The localized global distribution of lithium raises significant challenges for the use of Li-ion batteries (LIBs) in mass production. Seeking abundant and affordable alternatives is therefore crucial for a sustainable energy future. Na-ion battery (SIB) technology is one of the indisputable solutions, for instance, to power large-scale devices due to the accessibility of sodium resources and the potentially richer electrode chemistry compared with that of its lithium counterpart.[1−5] The expected low cost of Na-based systems can be an advantage for stationary applications, as a buffer energy storage to overcome grid fluctuations. The discovered sodium intercalation (insertion) compounds, that might outperform lithium intercalation compounds on pack level, have been the subject of discussion.[6] Since the increase of efforts and interest in SIBs in recent years, there has been rapid development in this field and different categories of cathode materials have been introduced up to now.[6−13] In Na-intercalation electrodes, compared to their Li equivalents, the working voltage is generally lower and the volume expansion larger. However, the power capability can vary depending on the crystal structure and diffusion channels.[2]

It can be admitted Na-intercalation chemistry has been less explored compared to Li-intercalation. Unstable Li-host structures may be reconsidered, where Na could be better accommodated into the structure.[14] Up to now, different structures have been introduced as cathode materials for SIBs. For instance, O3-type layered sodium transition metal oxides ($NaMO_2$, M refers to Ti, V, Cr, Mn, Fe, Co, or Ni) exhibit extensive intercalation chemistry, more than their Li counterparts,[6,15−18] which could be a promising class of cathode materials for SIB applications.[19,20] However, these materials suffer from severe capacity decay when the extraction of Na exceeds certain capacity limits. The capacity fade of $NaMO_2$ materials has been associated with irreversible structural transitions at the end of the full Na extraction, mainly with respect to transition metal migration and possible water/CO_2 intercalation into the Na layer.[19,21−24] In both cases, the Na diffusion channels are presumably blocked, resulting in a reduced degree of intercalation according to kinetic considerations.[25−27]

A number of recent studies on sodium intercalation compounds have focused on earth abundant and, hence, low-cost transition metals, especially manganese. For instance, layered Na_xMnO_2 compounds, α-$NaMnO_2$, which exhibits a monoclinic distortion of the O3 crystal structure (ABC oxygen

Received: September 23, 2022
Accepted: December 2, 2022

https://doi.org/10.1021/acsmaterialslett.2c00906
ACS Materials Lett. 2023, 5, 125−132

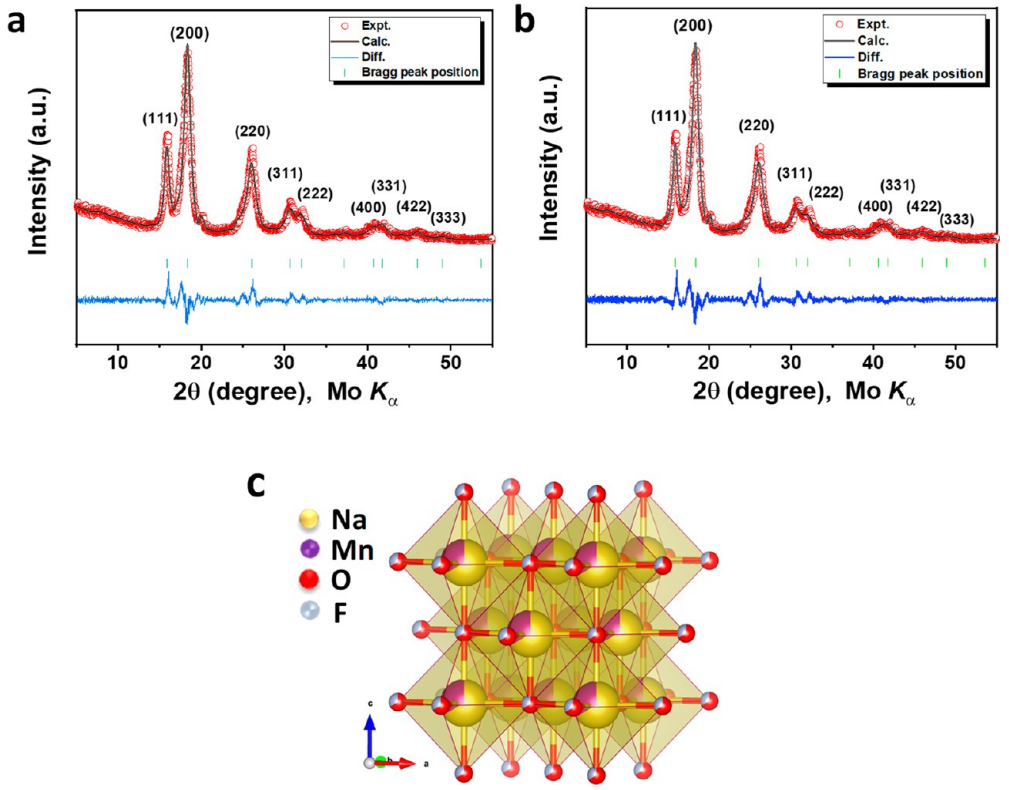

Figure 1. X-ray diffraction pattern and results of Rietveld refinement of a cubic rock salt phase (space group $Fm\bar{3}m$) for NMOF1 (a) and NMOF2 (b) and schematic illustration (c) of the crystal structure of the DRS phase.

stacking), and P2−$Na_{0.67}MnO_2$ (ABBA oxygen stacking) have been widely studied as sodium positive electrode materials.[28−30] A variety of stable manganese-based oxides exist, which are composed of one-, two-, or three-dimensionally connected sites for alkali metal intercalations,[31] for instance, electrochemical Na intercalation into spinel λ-$MnO_{2.86}$. When Na ions are inserted into λ-MnO_2 at the first discharge, the spinel phase is shown to transform to a new layered structure. After this irreversible phase transition, almost 0.6 Na ions could be reversibly cycled.[32]

Na-rich disordered rock salt (DRS) compounds are a new class of cathode materials, which have been investigated recently.[33,34] Up to now several compositions based on Mn, Ti, and Nb have been introduced;[33,34] however, all Na rich (DRS) structures suffer from cycling stability, owing to the reduced crystallinity, large volume change, and irreversible anionic redox activity especially during the charging (desodiation) process. Anionic substitution in Na-rich DRS could be applied as an efficient strategy to reduce the O-anionic redox activity, where more stable Na-rich composition can be targeted. Furthermore, the anion substitution, which influences the electronic state of the metal and crystal field, can tune the structure and the physicochemical properties as well, i.e., the changes in ion bonding and valence state can influence the structural stability. Hence, oxygen substitution by fluorine can be a good strategy to suppress the irreversible anionic redox process, as has been reported for other structures with improved capacity retention.[35] Nonetheless, the study of fluorinated Na-rich DRS materials with new chemistries is significantly lacking in literature; it is all the more required to investigate various SIB cathode materials given the actual energy context with proliferating gigafactories. It should be noted that this emerging class of DRS materials, which are at early stage of development, still suffer from fast capacity fading. However, their high potential in terms of structure and chemistry arouses interest for further study and investigation.

Here, we report a new synthesis of Mn-based oxyfluoride positive electrode materials with DRS structure for Na-ion battery applications. The Na-rich DRS oxyfluoride compounds were synthesized using high energy mechanochemical ball-milling, and their crystalline structure was characterized by powder X-ray diffraction (PXRD), being supported by Rietveld refinement analysis and electron microscopy (TEM/SEM). The electrochemical properties of the formulated cathodes were investigated using galvanostatic cycling, cyclic voltammetry (CV), electrochemical impedance spectroscopy (EIS) and *operando* X-ray absorption fine structure (XAFS). More experimental details are provided as Supporting Information (SI).

Figure 1 shows the powder XRD patterns for the two as-prepared Na_2MnO_2F (NMOF) compounds using two different precursors as a manganese source (Mn_2O_3 and MnO), in addition to Na_2O and NaF. NMOF1 was synthesized from Mn_2O_3 and NOMF2 from mixed oxides (Mn_2O_3 and MnO) to compensate the presence of Na_2O_2 impurity (assay 18−21%). For both compositions, the disordered rock salt structure was successfully formed using the mechanochemical synthesis approach.[36] The broadness of the diffraction peaks in the patterns is due to the nanocrystalline nature of the synthesized powders.[37] Rietveld refinement results confirm that all the compounds crystallize in $Fm\bar{3}m$ symmetry with a DRS structure, where Na and Mn cations occupy randomly the 4a Wyckoff octahedral sites and O and F anions occupy 4b Wyckoff sites. The refined lattice parameter was around 4.44 Å

https://doi.org/10.1021/acsmaterialslett.2c00906
ACS Materials Lett. 2023, 5, 125−132

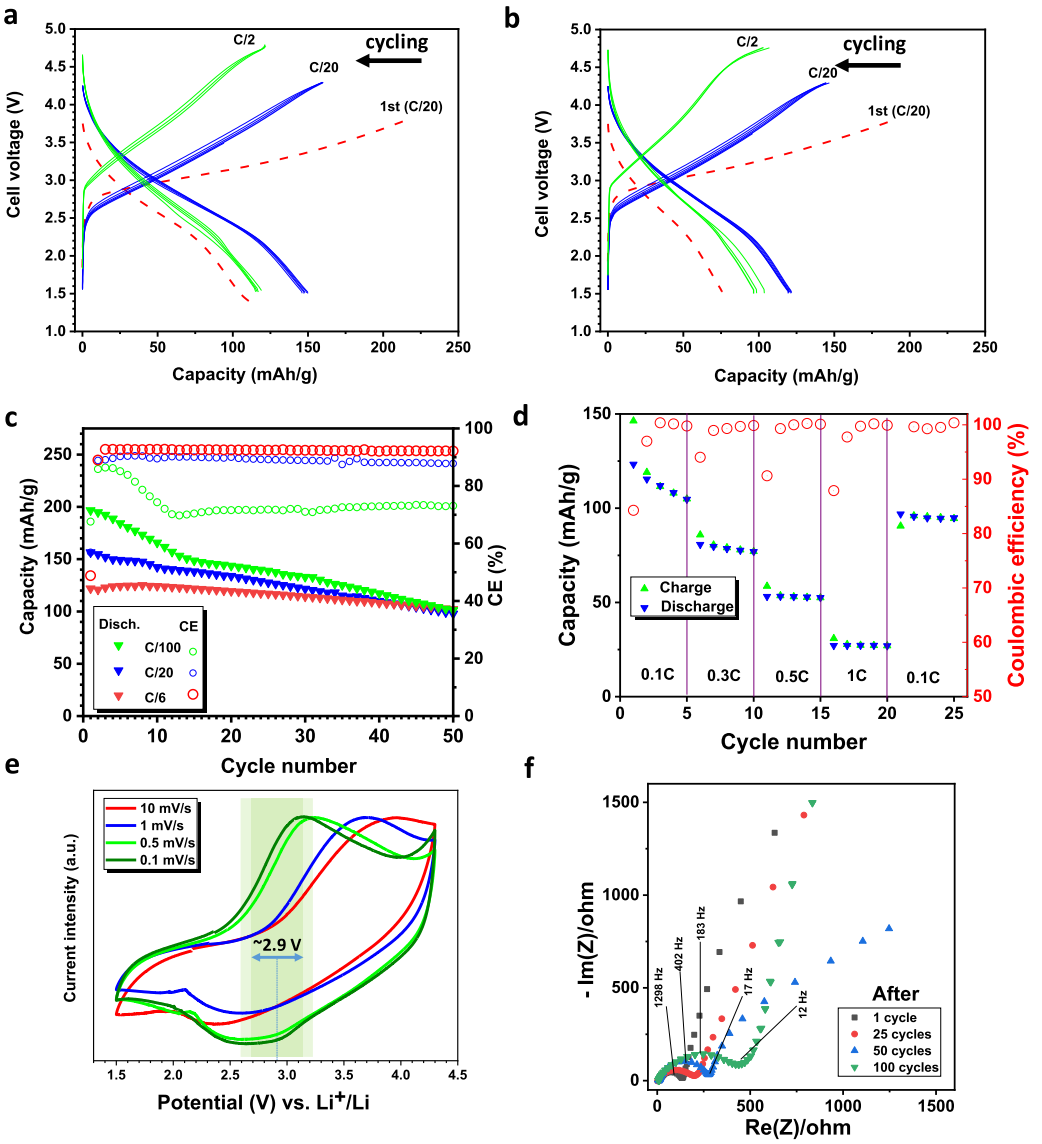

Figure 2. Voltage profiles (10th first cycles) of NMOF1 (a) and NMOF2 (b) at different cycling rates. Discharge capacity retention (c) of NMOF1 at different cycling rates (1.5−4.3 V window, 25 °C, CE = Coulombic Efficiency). Rate performance (d) and cyclic voltammograms (e) of NMOF1 sample. EIS profile (f) of NMOF1 sample cycled up to 100 cycles.

for MNOF1 and 4.46 Å for NMOF2. Additionally, it can be noticed that the I^{111}/I^{200} ratio in NMOF2 is slightly lower (0.44) compared to NMOF1 (0.53), which may be an indication of the formation of Na-rich NMOF2. A small reflection peak around 20° is visible in the diffraction pattern of both samples presumably related to unreacted NaF. More information on Rietveld refinement can be found in Table S1 (SI). Using the Williamson−Hall method, the crystallite size of both samples was calculated, as shown in Table S2, considering any contribution from microstrain. The morphology and particle size distribution obtained from SEM, and the related EDX elemental mapping of both samples are shown in Figure S1. Based on the SEM images the samples consist of fine particles that were agglomerated together into different sizes, leading to bigger particles. The average particle size of the samples is shown in Figure S1c and Table S2, indicating that the NMOF2 sample has relatively larger particle sizes. The EDX elemental mapping shown in Figure S1d,e reveals a particle constitution consistent with a homogeneous distribution of the elements. Regardless the EDX sensitivity to the elements present, the calculated cation and anions ratios are consistent with the stoichiometric composition in both samples.

Galvanostatic cycling in Na half-cells has been performed for the NMOF1 and NMOF2 mixed with conductive carbon additive. Both electrodes showed a similar sloping voltage profile (Figure 2a,b), with some difference at the early stage of cycling. The NMOF1-based electrode exhibited slightly higher first charge capacity (220 mAh g^{-1}) compared to the NMOF2-based electrode, corresponding to 1.25 Na^+ extracted from the structure. Note, at slow cycling rate (C/100, not shown) close to a steady state equilibrium, up to 1.7 Na^+ can be removed during the first desodiation. Additionally, the materials present good cyclability at a higher rate. One of the possible reasons of the capacity loss of the samples could be the irreversible anionic redox of oxygen, along with Mn dissolution. This is a known phenomenon in Li-DRS oxyfluoride cathode materials, which could be the case here as well.[38,39] The electrode which was directly synthesized from Mn_2O_3 only (NMOF1) provided better stability and capacity retention (Figure 2c). The increase

https://doi.org/10.1021/acsmaterialslett.2c00906
ACS Materials Lett. 2023, 5, 125−132

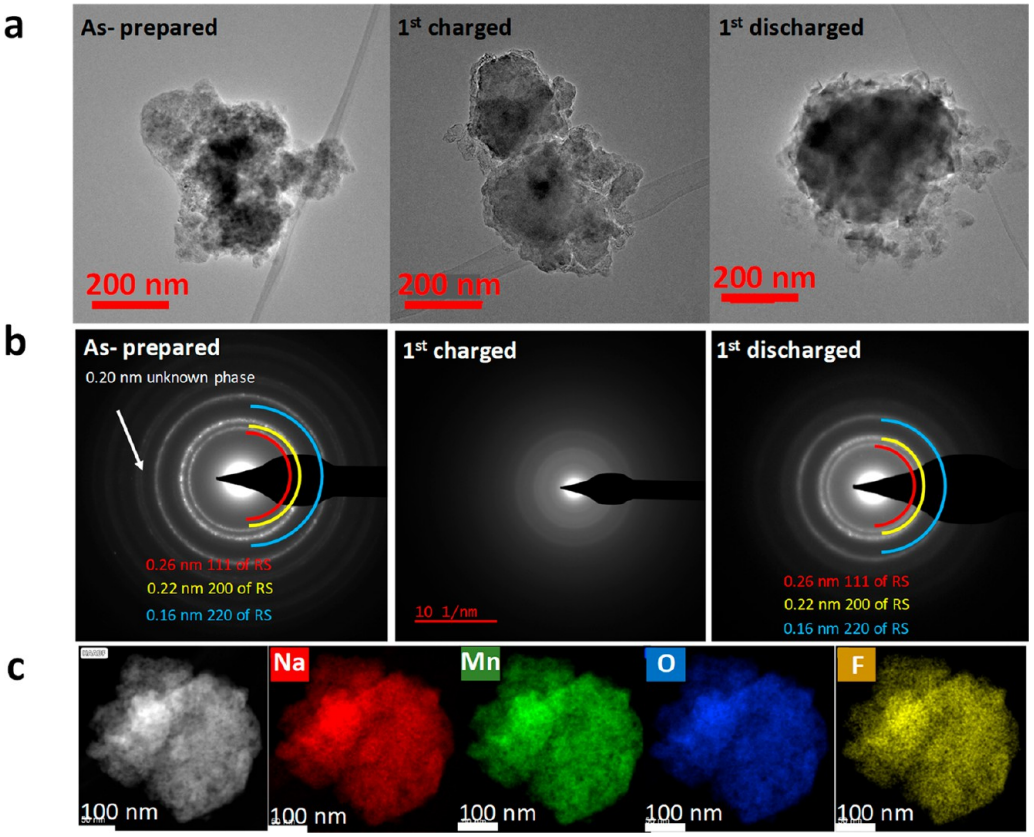

Figure 3. TEM images (a) and selected area electron diffraction (SAED) pattern (b) of as-prepared, 1st charged, and 1st discharged sample. HAADF STEM image (c) and the corresponding EDX elemental mapping of as-prepared sample, confirming the SEM observations.

of the rate contributed to the improvement of the cyclability. This suggests that electrolyte interaction with the cathode material could have occurred; however, owing to the small difference in Coulombic efficiency (CE) between 0.5 and 0.05 C, this seems to be less pronounced as compared to Li-rich DRS cathodes.[38,39] Figure 2d shows the rate performance of the NMOF1 cell conducted from 0.1 to 1 C and back to 0.1 C (1 C is defined as 352 mA g^{-1}) in the voltage range 1.5−4.2 V. Upon increase of the charge and discharge rates, the specific capacities decrease regularly. However, upon decrease of the rate returning to 0.1 C, the electrode was able to recover its starting capacity. This result suggests that the NMOF1 electrode may present low electronic conductivity and could afford rapid charge and discharge upon suitable surface modification.

Cyclic voltammetry (CV) results for the NMOF1 sample shown in Figure 2e consist of one redox process with an equilibrium potential around 2.9 V for Mn^{3+}/Mn^{4+}.[39] Upon scan rate variation, it can be confirmed from the linear E sweep transient method that the record of the currents indicated the presence of a limiting diffusion process at high scan rate, where the kinetic diffusion becomes slow. Electrochemical impedance spectra (Figure 2f) revealed that during cycling the resistive contributions from the different segments of the batteries such as sodium ion migration through the electrode surface film (R_{mt}) and the charge transfer resistance (R_{ct}) are increased by cycling.[40] The increase of semicircle diameter with cycling is in accordance with the continuous capacity fading. The initial value of R_{mt} + R_{ct} was 150 Ω, which increased to around 208, 285, and 482 Ω after 25, 50, and 100 cycles, respectively.

Similar to Li-rich materials, anionic redox reaction can contribute to trigger the Mn dissolution, as one critical issue for long-term cyclability. In order to probe the amount of Mn dissolved in the electrolyte and deposited on the anode (Na metal foil), ICP-OES analyses were conducted on the sodium foil extracted from the 150-cycled battery cells. The aim was to correlate the detected Mn in the anode side to the structural stability of the cathode in the presented configuration. As it is shown in Table S4, more than three times the amount of Mn could be detected for the NMOF2 cell than in the NMOF1 cell. This suggests that the latter has a higher structural stability in agreement with the observed capacity retention during cycling, while the NMOF2, though it could be a Na-rich compound, is probably destabilized by the presence of the additional MnO phase precursor. In the following, investigations are focused on the NMOF1 sample.

To further understand the morphology and elemental distribution and monitor the change in the crystal structure of the NMOF1 sample, TEM/EDX, SAED (selected area electron diffraction), and PDF (pair distribution function) analyses were performed on the as-prepared, first charged, and first discharged samples. The morphology of the as-prepared sample was characterized by the STEM (Figure 3a). It shows that the particle size of the sample randomly differs from tens of nanometers to a few micrometers. Also the morphology of the charged and discharged samples changed noticeably.

For the as-prepared sample, the corresponding SAED pattern in Figure 3b presents bright circular rings, which correspond to the (111), (200), and (220) planes of a rock-salt structure ($Fm\bar{3}m$), in good agreement with the analysis of XRD results in Figure 1. However, in the charged sample after the

https://doi.org/10.1021/acsmaterialslett.2c00906
ACS Materials Lett. 2023, 5, 125−132

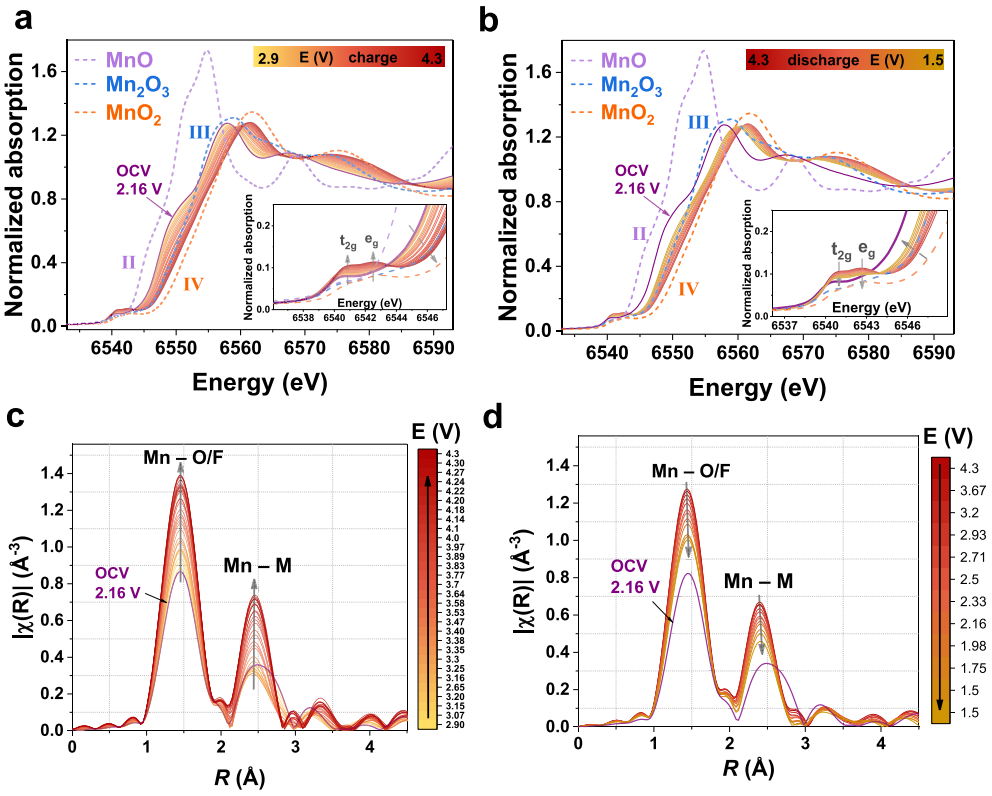

Figure 4. Normalized Mn K-edge XANES of NMOF1 during the first charge (a) and discharge (b) from the *operando* XAFS measurement; insets highlight the pre-edge region. Fourier transform of k^2-weighted $\chi(k)$ spectra obtained from the charge (c) and discharge (d).

desodiation process, the long-range ordering of the crystal structure of the as-prepared sample was destroyed, in agreement with the observed XRD loss of crystallinity of the same sample (not shown). Interestingly, with sodiation and discharging the sample, the initial crystal structure of as-prepared sample reappears. As shown in the diffraction pattern (Figure 3b), all the diffraction rings could be indexed by the initial rock salt structure. However, the diffraction rings are broader than those in the diffraction pattern of as-prepared sample, which may suggest an increased diffuse scattering owing to presence of a nanocrystalline phase. Similar structural behavior has been reported for Li_2VO_2F using X-ray total scattering data,[41] with more or less amorphous diffuse scattering at the charged state.

The EDX mapping of all the samples shows a homogeneous elemental distribution (Figure 3c and Figure S2). We have calculated the elemental ratios of Na and Mn for the as-prepared sample and the charged samples (Table S5). The Na/Mn ratio of the selected area for the as-prepared sample is ~1.75 lower than 2, which points out the possible formation of a hypo-stoichiometric phase. After desodiation, the ratio decreased to ~0.66, a sign of a successful desodiation process.

The PDF analysis was carried out to study the amorphous structure of the first charged sample (Figure S3). The PDF of the as-prepared sample show good agreement with the simulated pattern resulting from XRD of the sample. After desodiation, the PDF shows clear change. The first peak moves to lower "*r*" indicating the Na/Mn−O/F distance becomes shorter. Compared with the possible candidates in our system (MnO_2, Mn_2O_3, MnF_4, Na_2O, and NaF), the first peak of the first charged sample could be attributed to the Mn-anion (O/F) bound distance. The PDF analysis of the first charged sample cannot be indexed by any of the above single candidates. However, we cannot figure out if the product after desodiation is single phase $Na_{2-x}MnO_2F$ or a complex mixture of different phases. The PDF of the first discharged sample, shown in Figure S3, shows good agreement with that of the as-prepared sample indicating the reversibility of the sample during battery cycling. For better understanding of the reversibility of the Mn redox during cycling, EELS spectra of the Mn L-edge were collected for all the samples, shown in Figure S4a. The results showed that during battery cycling, the Mn was first oxidized (desodiation) and then reduced back (sodiation), in agreement with electrochemical data.

To better explore the different electrochemistry, the redox mechanism was probed using X-ray absorption spectroscopy (XAS). *Operando* Mn K-edge XAFS was performed on the NMOF1 powder electrode in the initial charge−discharge cycle between 1.5 and 4.3 V at a rate of C/5 (Figure S5). XANES fingerprinting with Mn standards demonstrated a gradual edge shift toward higher energy during charge from open circuit voltage (OCV, 2.16 V) to 4.3 V (Figure 4a) and reversibly to lower energy during the discharge process from 4.3 down to 1.5 V (Figure 4b), reflecting the Mn oxidation by desodiation and the reduction upon sodiation. Consistently, the two pre-edge peaks representing the 1s → 3d (1s → t_{2g} and 1s → e_g) quadrupole transitions exhibited increasing intensity during desodiation. This corresponds to the rising number of available empty 3d energy levels of Mn cations at higher oxidation state. In return, a reverse trend was observed upon discharge. In Figure 4c,d, the magnitude of Fourier transform $|\chi(R)|$ of k^2-weighted $\chi(k)$ is represented during both charging and discharging of the material. During charge, the increasing intensity of the first and second shell peaks indicated the

https://doi.org/10.1021/acsmaterialslett.2c00906
ACS Materials Lett. 2023, 5, 125−132

increase of the local ordering by the release of Na^+ out of the structure. Upon discharge and sodiation, the magnitudes of both coordination shells decreased significantly with increasing local disordering by Na^+ entering into the lattice but not completely reversibly toward the initial OCV states.

To verify the relative cycling stability, cells were charged (1 charge) and discharged (1 full cycle) at a slow rate (C/100), followed by 2 h floating voltage to ensure complete redox reaction. Afterward, the powder cathodes were extracted, washed with DMC to remove the electrolyte residue, and dried overnight under vacuum before being analyzed with *ex situ* XANES. Figure S6 shows the Mn K-edge of the NOMF1 electrodes at different states of charge. Both pristine and discharged NMOF1 showed an average Mn oxidation state of 3+, while the Mn in fully charged (4.3 V) NOMF1 exhibited a 4+ state. This confirms the kinetic issue due to insufficient desodiation/sodiation with C/5 rate during *operando* measurement, with relatively high electrode loading mass leading to lower average Mn oxidation state.

EXAFS fitting was performed for the first coordination shell Mn−O/F, as shown in Figure S7 and Table S6. The average interatomic distance *R* between the central Mn and the nearest O and F ligands in the octahedral coordination showed a gradual decrease with charging and an increase with discharging (Figure 5a). This evolution is in agreement with

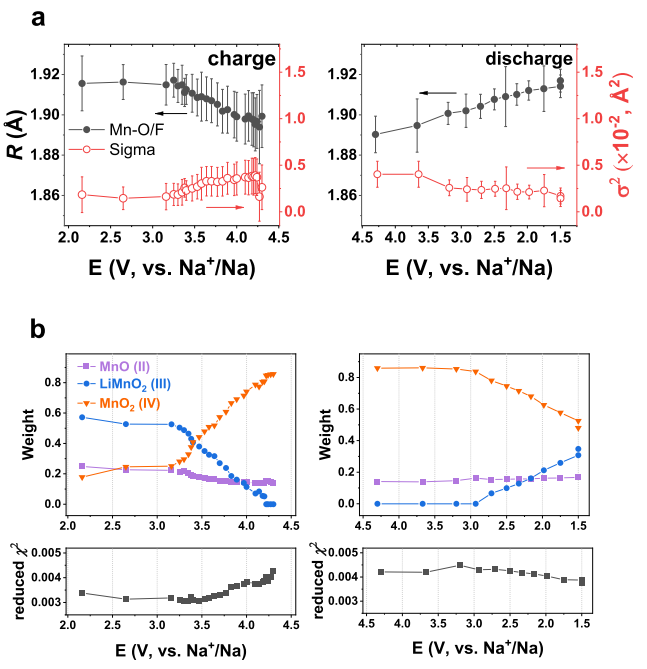

Figure 5. Evolution of interatomic distance *R* (a) between the central absorbing Mn and the first coordination shell, as well as the disordering factor σ^2 obtained from the EXAFS fitting. Results of linear combination fitting of the XANES spectra (b) using $Mn^{II}O$, $LiMn^{III}O_2$ and $Mn^{IV}O_2$ as standards; reduced χ^2 values represent the uncertainties and show no significant change between the fits.

the change of Mn oxidation states and demonstrates the local structural contraction and expansion caused by Na extraction and insertion, respectively. However, the *R* change is relatively small, for instance, about 0.03 Å from 4.3 to 1.5 V during discharge. In addition, the disordering factors σ^2 showed only a weak evolution.

Figure 5b shows the results of linear combination fit (LCF) of XANES spectra. Principle components analysis (PCA) suggested these spectra might have more than 5 components but only three of them have a weight ratio larger than 0.001, as shown in Figure S8a,b. In total, these three main components counted for 99.8% of the variation in the data, which was also enough to match the experimental spectra (Figure S8c). Nevertheless, in order to track the evolution of the oxidation state, experimental spectra measured from three reference standards, MnO, $LiMnO_2$, and MnO_2, were used for LCF fitting (Figure S8d), and here a synthesized disordered rock salt ($Fm\bar{3}m$) $LiMnO_2$ was selected as Mn^{III} standard instead of Mn_2O_3. For both charging and discharging, the main varying components were Mn^{III} and Mn^{IV} in these intermediate states, and the remaining Mn^{II} seemed to be less redox-active. During charge, the amount of Mn^{IV} gradually increased from a small weight fraction <0.2 at OCV to a dominating >0.8 at full charge 4.3 V, along with the decrease of Mn^{III} from <0.6 to almost null, suggesting a $Mn^{3+/4+}$ redox behavior reached at rather fast rate for this *operando* cell. By return backward, the relative amount of each component exhibited weaker change during the discharge from 4.3 to 1.5 V. The Mn^{IV} component decreases from >0.8 to about 0.5 and Mn^{III} increases from 0 to around 0.3, while Mn^{II} showed no significant variation. As a result of the overall high Mn^{IV} ratio, the average Mn oxidation state in fully discharged 1.5 V was still higher than that of the initial OCV (2.2 V), with a higher edge energy position, presumably owing to kinetic cell issues at high rate as discussed earlier.

Briefly, a new Na-rich Mn-based DRS oxyfluoride Na_2MnO_2F has been synthesized by solid-state mechanochemistry for consideration as cathode material for next-generation rechargeable SIBs. In this system, Na and Mn ions occupy randomly the octahedral sites (4a) in a *cubic-close packed* (*ccp*) lattice with 23% larger cell volume compared to its Li homologue. The formulated electrodes have been electrochemically tested, where up to 1.7 Na^+ can be extracted from the structure at slow cycling rate during charge, corresponding to an initial capacity of 298 mAh g^{-1}. The results showed that the electrodes preserve a capacity of 100 mAh g^{-1} over 50 cycles and stable Coulombic efficiency at fast rates without any cell optimization.

The Mn K-edge XANES proved that the manganese undergoes a single Mn^{3+}/Mn^{4+} redox reaction during charge/discharge process, in agreement with cyclic voltammetry. The loss of crystallinity after desodiation, and its reversion back after full cycling remains unclear, which needs to be investigated further for this new category of materials. However, *operando* XAFS demonstrated the Mn redox evolution upon cycling, and the Fourier transform representation showed the increase/decrease of the local ordering upon Na^+ extraction/insertion. This research is an additional input to accelerate the evolution of new systems and chemistries for the forthcoming SIBs technologies.

■ ASSOCIATED CONTENT

Supporting Information

The Supporting Information is available free of charge at https://pubs.acs.org/doi/10.1021/acsmaterialslett.2c00906.

Detailed experimental section. Electron microscopy images of the different samples before and after cycling. PDF analysis and EELS spectra as a function of state of

https://doi.org/10.1021/acsmaterialslett.2c00906
ACS Materials Lett. 2023, 5, 125−132

charge. *Operando* cycling profile and *ex-situ* XANES of samples obtained at slow rate. Additional EXAFS data and PCA analysis, and examples of shell fitting. Tables containing the corresponding information on structural and fitting parameters, elemental quantifications and energy grid of the extracted Mn K-edge spectra (PDF)

AUTHOR INFORMATION

Corresponding Author

Abdel El Kharbachi − *Helmholtz Institute Ulm (HIU), 89081 Ulm, Germany;* orcid.org/0000-0003-4332-1544; Email: kharbachi@kit.edu

Authors

Yasaman Shirazi Moghadam − *Helmholtz Institute Ulm (HIU), 89081 Ulm, Germany*

Yang Hu − *Helmholtz Institute Ulm (HIU), 89081 Ulm, Germany;* orcid.org/0000-0001-6864-6498

Kai Wang − *Institute of Nanotechnology, Karlsruhe Institute of Technology (KIT), 76021 Karlsruhe, Germany*

Stéphanie Belin − *SOLEIL Synchrotron, F-91192 Gif-sur-Yvette, France*

Maximilian Fichtner − *Helmholtz Institute Ulm (HIU), 89081 Ulm, Germany; Institute of Nanotechnology, Karlsruhe Institute of Technology (KIT), 76021 Karlsruhe, Germany;* orcid.org/0000-0002-7127-1823

Complete contact information is available at: https://pubs.acs.org/10.1021/acsmaterialslett.2c00906

Author Contributions

The manuscript was written through contributions of all authors. All authors have given approval to the final version of the manuscript. CRediT: **Yasaman Shirazi Moghadam** conceptualization, data curation, formal analysis, investigation, methodology, writing-original draft; **Abdel El Kharbachi** conceptualization, data curation, supervision, writing-review & editing; **Yang Hu** data curation, formal analysis, writing-review & editing; **Kai Wang** data curation, formal analysis; **Stéphanie Belin** data curation, methodology, writing-review & editing; **Maximilian Fichtner** funding acquisition, supervision.

Funding

The German Research Foundation (DFG) under Project ID 390874152 (POLiS Cluster of Excellence, EXC 2154).

Notes

The authors declare no competing financial interest.

ACKNOWLEDGMENTS

This work contributes to the research performed at CELEST (Center for Electrochemical Energy Storage Ulm-Karlsruhe) and was funded by the German Research Foundation (DFG) under Project ID 390874152 (POLiS Cluster of Excellence, EXC 2154). The synchrotron XAFS were conducted at the ROCK beamline of the SOLEIL synchrotron (proposal number 20210779) and supported by a public grant overseen by the French National Research Agency (ANR) as part of the "Investissements d'Avenir" program (reference ANR-10-EQPX-45). The authors also thank the KNMFi (Karlsruhe Nano Micro Facility).

REFERENCES

(1) Palomares, V.; Casas-Cabanas, M.; Castillo-Martínez, E.; Han, M. H.; Rojo, T. Update on Na-based battery materials. A growing research path. *Energy Environ. Sci.* **2013**, *6*, 2312−2337.

(2) Kim, S. W.; Seo, D. H.; Ma, X.; Ceder, G.; Kang, K. Electrode materials for rechargeable sodium-ion batteries: potential alternatives to current lithium-ion batteries. *Adv. Energy Mater.* **2012**, *2*, 710−721.

(3) Ellis, B. L.; Nazar, L. F. Sodium and sodium-ion energy storage batteries. *Curr. Opin. Solid State Mater. Sci.* **2012**, *16*, 168−177.

(4) Slater, M. D.; Kim, D.; Lee, E.; Johnson, C. S. Sodium-ion batteries. *Adv. Funct. Mater.* **2013**, *23*, 947−958.

(5) Yabuuchi, N.; Kubota, K.; Dahbi, M.; Komaba, S. Research development on sodium-ion batteries. *Chem. Rev.* **2014**, *114*, 11636−11682.

(6) Billaud, J.; Clément, R. J.; Armstrong, A. R.; Canales-Vázquez, J.; Rozier, P.; Grey, C. P.; Bruce, P. G. *β*-NaMnO2: a high-performance cathode for sodium-ion batteries. *J. Am. Chem. Soc.* **2014**, *136*, 17243−17248.

(7) Xu, J.; Lee, D. H.; Clément, R. l. J.; Yu, X.; Leskes, M.; Pell, A. J.; Pintacuda, G.; Yang, X.-Q.; Grey, C. P.; Meng, Y. S. Identifying the critical role of Li substitution in P2−Na x [Li y Ni z Mn1−y−z] O2 (0< x, y, z< 1) intercalation cathode materials for high-energy Na-ion batteries. *Chem. Mater.* **2014**, *26*, 1260−1269.

(8) Ellis, B.; Makahnouk, W.; Makimura, Y.; Toghill, K.; Nazar, L. A multifunctional 3.5 V iron-based phosphate cathode for rechargeable batteries. *Nat. Mater.* **2007**, *6*, 749−753.

(9) Ma, J.; Bo, S.-H.; Wu, L.; Zhu, Y.; Grey, C. P.; Khalifah, P. G. Ordered and disordered polymorphs of Na (Ni2/3Sb1/3) O2: honeycomb-ordered cathodes for Na-ion batteries. *Chem. Mater.* **2015**, *27*, 2387−2399.

(10) Li, X.; Wu, D.; Zhou, Y.-N.; Liu, L.; Yang, X.-Q.; Ceder, G. O3-type Na (Mn0. 25Fe0. 25Co0. 25Ni0. 25) O2: A quaternary layered cathode compound for rechargeable Na ion batteries. *Electrochem. Commun.* **2014**, *49*, 51−54.

(11) Liu, J.; Chang, D.; Whitfield, P.; Janssen, Y.; Yu, X.; Zhou, Y.; Bai, J.; Ko, J.; Nam, K.-W.; Wu, L.; et al. Ionic conduction in cubic Na3TiP3O9N, a secondary Na-ion battery cathode with extremely low volume change. *Chem. Mater.* **2014**, *26*, 3295−3305.

(12) Yabuuchi, N.; Kajiyama, M.; Iwatate, J.; Nishikawa, H.; Hitomi, S.; Okuyama, R.; Usui, R.; Yamada, Y.; Komaba, S. P2-type Nax [Fe1/2Mn1/2] O2 made from earth-abundant elements for rechargeable Na batteries. *Nat. Mater.* **2012**, *11*, 512−517.

(13) Kim, D.; Lee, E.; Slater, M.; Lu, W.; Rood, S.; Johnson, C. S. Layered Na [Ni1/3Fe1/3Mn1/3] O2 cathodes for Na-ion battery application. *Electrochem. Commun.* **2012**, *18*, 66−69.

(14) Nayak, P. K.; Yang, L.; Brehm, W.; Adelhelm, P. From lithium-ion to sodium-ion batteries: advantages, challenges, and surprises. *Angew. Chem., Int. Ed.* **2018**, *57*, 102−120.

(15) Lu, Z.; MacNeil, D.; Dahn, J. Layered cathode materials Li [Ni x Li (1/3− 2x/3) Mn (2/3− x/3)] O 2 for lithium-ion batteries. *Electrochem. Solid-State Lett.* **2001**, *4*, A191.

(16) Ohzuku, T.; Makimura, Y. Layered lithium insertion material of LiNi1/2Mn1/2O2: a possible alternative to LiCoO2 for advanced lithium-ion batteries. *Chem. Lett.* **2001**, *30*, 744−745.

(17) Spahr, M. E.; Novák, P.; Schnyder, B.; Haas, O.; Nesper, R. Characterization of layered lithium nickel manganese oxides synthesized by a novel oxidative coprecipitation method and their electrochemical performance as lithium insertion electrode materials. *J. Electrochem. Soc.* **1998**, *145*, 1113.

(18) MacNeil, D.; Lu, Z.; Dahn, J. R. Structure and electrochemistry of Li [Ni x Co1− 2x Mn x] O 2 (0⩽ x⩽ 1/2). *J. Electrochem. Soc.* **2002**, *149*, A1332.

(19) Yabuuchi, N.; Yoshida, H.; Komaba, S. Crystal structures and electrode performance of alpha-NaFeO2 for rechargeable sodium batteries. *Electrochemistry* **2012**, *80*, 716−719.

(20) Komaba, S.; Takei, C.; Nakayama, T.; Ogata, A.; Yabuuchi, N. Electrochemical intercalation activity of layered NaCrO2 vs. LiCrO2. *Electrochem. Commun.* **2010**, *12*, 355−358.

(21) Didier, C.; Guignard, M.; Denage, C.; Szajwaj, O.; Ito, S.; Saadoune, I.; Darriet, J.; Delmas, C. Electrochemical Na-Deintercalation from NaVO2. *Electrochem. Solid-State Lett.* **2011**, *14*, A75.
(22) Wu, D.; Li, X.; Xu, B.; Twu, N.; Liu, L.; Ceder, G. NaTiO 2: a layered anode material for sodium-ion batteries. *Energy Environ. Sci.* **2015**, *8*, 195−202.
(23) Maazaz, A.; Delmas, C.; Hagenmuller, P. A study of the Na x TiO2 system by electrochemical deintercalation. *J. Incl. Phenom.* **1983**, *1*, 45−51.
(24) Komaba, S.; Nakayama, T.; Ogata, A.; Shimizu, T.; Takei, C.; Takada, S.; Hokura, A.; Nakai, I. Electrochemically reversible sodium intercalation of layered NaNi0. 5Mn0. 5O2 and NaCrO2. *ECS Trans.* **2009**, *16*, 43.
(25) Buchholz, D.; Chagas, L. G.; Vaalma, C.; Wu, L.; Passerini, S. Water sensitivity of layered P2/P3-Na x Ni 0.22 Co 0.11 Mn 0.66 O 2 cathode material. *J. Mater. Chem. A* **2014**, *2*, 13415−13421.
(26) Duffort, V.; Talaie, E.; Black, R.; Nazar, L. F. Uptake of CO2 in layered P2-Na0. 67Mn0. 5Fe0. 5O2: insertion of carbonate anions. *Chem. Mater.* **2015**, *27*, 2515−2524.
(27) Lu, Z.; Dahn, J. Intercalation of Water in P2, T2 and O2 Structure A z [Co x Ni1/3-x Mn2/3] O2. *Chem. Mater.* **2001**, *13*, 1252−1257.
(28) Ma, X.; Chen, H.; Ceder, G. Electrochemical properties of monoclinic NaMnO2. *J. Electrochem. Soc.* **2011**, *158*, A1307.
(29) Mendiboure, A.; Delmas, C.; Hagenmuller, P. Electrochemical intercalation and deintercalation of NaxMnO2 bronzes. *J. Solid State Chem.* **1985**, *57*, 323−331.
(30) Caballero, A.; Hernan, L.; Morales, J.; Sanchez, L.; Pena, J. S.; Aranda, M. Synthesis and characterization of high-temperature hexagonal P2-Na 0.6 MnO 2 and its electrochemical behaviour as cathode in sodium cells. *J. Mater. Chem.* **2002**, *12*, 1142−1147.
(31) Wei, W.; Cui, X.; Chen, W.; Ivey, D. G. Manganese oxide-based materials as electrochemical supercapacitor electrodes. *Chem. Soc. Rev.* **2011**, *40*, 1697−1721.
(32) Tarascon, J.; Guyomard, D.; Wilkens, B.; Mc Kinnon, W.; Barboux, P. Chemical and electrochemical insertion of Na into the spinel λ-MnO2 phase. *Solid State Ion.* **1992**, *57*, 113−120.
(33) Sato, K.; Nakayama, M.; Glushenkov, A. M.; Mukai, T.; Hashimoto, Y.; Yamanaka, K.; Yoshimura, M.; Ohta, T.; Yabuuchi, N. Na-excess cation-disordered rocksalt oxide: Na1. 3Nb0. 3Mn0. 4O2. *Chem. Mater.* **2017**, *29*, 5043−5047.
(34) Kobayashi, T.; Zhao, W.; Rajendra, H. B.; Yamanaka, K.; Ohta, T.; Yabuuchi, N. Nanosize Cation-Disordered Rocksalt Oxides: Na2TiO3−NaMnO2 Binary System. *Small* **2020**, *16*, 1902462.
(35) Deng, D. Transition Metal Oxyfluorides for Next-Generation Rechargeable Batteries. *ChemNanoMat* **2017**, *3*, 146−159.
(36) Freire, M.; Kosova, N. V.; Jordy, C.; Chateigner, D.; Lebedev, O.; Maignan, A.; Pralong, V. A new active Li−Mn−O compound for high energy density Li-ion batteries. *Nat. Mater.* **2016**, *15*, 173−177.
(37) Baur, C.; Kallquist, I.; Chable, J.; Chang, J. H.; Johnsen, R. E.; Ruiz-Zepeda, F.; Ateba Mba, J. M.; Naylor, A. J.; Garcia-Lastra, J. M.; Vegge, T.; et al. Improved cycling stability in high-capacity Li-rich vanadium containing disordered rock salt oxyfluoride cathodes. *J. Mater. Chem. A* **2019**, *7*, 21244−21253.
(38) Shirazi Moghadam, Y.; Dinda, S.; El Kharbachi, A.; Melinte, G.; Kübel, C.; Fichtner, M. Structural and Electrochemical Insights from the Fluorination of Disordered Mn-Based Rock Salt Cathode Materials. *Chem. Mater.* **2022**, *34*, 2268−2281.
(39) Shirazi Moghadam, Y.; El Kharbachi, A.; Diemant, T.; Melinte, G.; Hu, Y.; Fichtner, M. Toward Better Stability and Reversibility of the Mn4+/Mn2+ Double Redox Activity in Disordered Rocksalt Oxyfluoride Cathode Materials. *Chem. Mater.* **2021**, *33*, 8235−8247.
(40) Cambaz, M. A.; Vinayan, B. P.; Gesswein, H.; Schiele, A.; Sarapulova, A.; Diemant, T.; Mazilkin, A.; Brezesinski, T.; Behm, R. J.; Ehrenberg, H.; et al. Oxygen Activity in Li-Rich Disordered Rock-Salt Oxide and the Influence of LiNbO3 Surface Modification on the Electrochemical Performance. *Chem. Mater.* **2019**, *31*, 4330−4340.
(41) Baur, C.; Lăcătuşu, M.-E.; Fichtner, M.; Johnsen, R. E. Insights into Structural Transformations in the Local Structure of Li2VO2F Using Operando X-ray Diffraction and Total Scattering: Amorphization and Recrystallization. *ACS Appl. Mater. Interfaces* **2020**, *12*, 27010−27016.

https://doi.org/10.1021/acsmaterialslett.2c00906
ACS Materials Lett. 2023, 5, 125−132